IEEE Robotics and Automation Letters (RA-L) paper, presented at ICRA 2026, Vienna, Austria. Cite as RA-L paper.

TCS Jumper: A Bio-Inspired Jumping Robot Featuring High Energy Density via Synergistic Deformation

Yang Yang, *Student Member, IEEE*, DeYi Kong, YuLiang Wei, JunKui Zhong, and ZhengGuo Su

***Abstract*—Maximizing the energy density of springs is a key consideration in designing spring-driven jumping robots. Inspired by the synergistic deformation mechanism of springtails, which involves the coupled action of rotational and bending deformations in their furcula, we created the TCS Jumper (Torsion springs and Carbon-fiber Strips actuated jumping robot) prototype, combining double-torsion springs (linear elastic elements) and carbon-fiber strips (nonlinear elastic elements) in series. A unified nonlinear axial force model was established by coupling Timoshenko's large deformation theory with linear torsion spring mechanics, revealing dynamic strain coordination that enables mechanical compatibility between elastic elements with distinct elastic deformation characteristics. This model achieved $<4.4\%$ force deviation across torsion angles from 0 to $\pi/2$ rad, demonstrating quasi-static elastic deformation control. Experimental validation showed the novel SEA stores 28J energy (140J/kg density) and enables the 345g TCS Jumper to achieve 3.5m vertical jump height with 52.4J/kg system energy density and 65.4% gravitational potential energy conversion efficiency. This study presents a framework for designing high-performance, spring-driven robots with heterogeneous elastic systems.**

***Index Terms*—Jumping robot, springtail inspired, synergistic energy release, series elastic actuator.**

I. Introduction

SPRING jumping robots are well-suited for applications requiring high mobility in complex environments, such as terrain exploration [1], disaster rescue [2], and planetary exploration [3], owing to their inherent obstacle-crossing capabilities and high energy efficiency [4]. The performance of these robots is fundamentally determined by the energy storage and release characteristics of elastic actuators [5]. Traditional designs employing a single elastic element, such as a linear or torsion spring, often exhibit low energy density and suboptimal energy conversion efficiency [6], [7], [8], limiting their ability to meet high performance of jumping requirements [9].

To overcome these limitations, recent research has focused on coupling heterogeneous elastic elements to enhance the elastic potential energy storage of the elastic actuator system. This approach has yielded remarkable performance gains. For instance, by series coupling carbon fiber and rubber, Hawkes et al. developed a robot capable of a 32.9 m jump height, far exceeding that of biological jumpers [10]. Similarly, Jung et al. increased the energy density of the JumpRoACH robot to 41.1 J/kg by series combining linear and torsion springs [11], [12], while Yamada et al. improved storage density by 18% over pure bending by integrating elastic strip bending, torsion, and snap-through buckling [13], [14]. Zhao et al. developed the MSU tailbot using a single motor-driven steering mechanism to achieve a jump height of 143 cm with a 25-g robot [15], [16], [17]. Other successful implementations include series coupling torsion springs with NiTi alloy plates to achieve a 1.23 m jumper [18] and employing hybrid series–parallel elastic mechanisms in frog-inspired designs to reach a 1.3 m height with a storage capacity of 18.1 J/kg [19]. We provided a brief review of the major achievements of jumping robots in recent decades, which are summarized in Table I.

Bio-inspired designs have unlocked new energy transfer paradigms. Dong et al. achieved 60.5 cm aquatic and 3.85 m terrestrial jumps in a 27 cm frog-inspired robot via a 1-DOF four-bar linkage with rubber-band energy storage and frog-shaped paddles [23]. Xu et al. achieved 30 cm vertical jumps and 70 cm distance in a 10 cm, 60 g locust-inspired robot via a Stephenson six-bar leg mechanism and two-step optimization,

TABLE I
Performance Comparison of Spring-Jumping Robots

Jumping robot	Mass(g)	Jumping height (cm)	Energy capacity (J/kg)
Jumping robots [20]	205.6	158	24
Engineered Jumper [10]	30.37	3290	1075
JumpRoACH [12]	42.6	275	30.9
Salto-1P [1], [21]	98	125	12.2
Multimo-Bat [22]	115.6	305	54.9
TCS-Jumper	**534**	**350**	**52.4**

Received 30 July 2025; accepted 20 November 2025. Date of publication 25 December 2025; date of current version 6 January 2026. This article was recommended for publication by Associate Editor J. Legrand and Editor X. Liu upon evaluation of the reviewers' comments. This work was supported in part by the National Natural Science Foundation of China under Grant 12304503, in part by the Scientific Research Project of Universities in Anhui Province, China, under Grant 2024AH051102, and in part by USTC Rising Talents Fund under Grant CY2023G007. *(Corresponding authors: DeYi Kong; YuLiang Wei.)*

Yang Yang is with the Hefei Institutes of Physical Science, Chinese Academy of Sciences, Hefei 230031, China, also with the University of Science and Technology of China, Hefei 230026, China, and also with Anqing Normal University, Anqing 246133, China (e-mail: yangyang17@mail.ustc.edu.cn).

DeYi Kong, YuLiang Wei, JunKui Zhong, and ZhengGuo Su are with the Hefei Institutes of Physical Science, Chinese Academy of Sciences, Hefei 230031, China (e-mail: kongdy@iim.ac.cn; weiyl@iim.ac.cn; zhongjk@iim.ac.cn; suzhengguo0227@163.com).

Digital Object Identifier 10.1109/LRA.2025.3648607

IEEE Robotics and Automation Letters (RA-L) paper, presented at ICRA 2026, Vienna, Austria. Cite as RA-L paper.

enabling stable, non-flipping elastic energy storage/release [24]. Sato et al. achieved 544 mm vertical jumps in a legged robot via feline-inspired upper-lower-leg bi-articular MTCs [25].

Despite these empirical successes, the nonlinear mechanical coupling mechanisms in spring systems remain insufficiently understood. For instance, while the work multiplication principle proposed by Hawkes et al. achieved record-breaking jump heights, the force–displacement behavior of its hybrid spring system was obtained via simulation, lacking an analytical model to reveal the intrinsic mechanical coupling between components [10]. Serrano et al. realized walking-jumping multimodal locomotion using shape memory alloy actuation; their modeling approach simplified spring elements as linear torsional springs, with key parameters ultimately determined through experimental data [26]. Although the jumping beetle-inspired Tumro robot by Pan et al. [7] demonstrated the energy storage advantages of biological elastic ligaments, the force–displacement relationship of its spring system still relied on experimental measurement and lacked theoretical predictability. Zhao et al. derived the force–displacement relation for an elastic band using large deformation theory via a simplified analytical model, yet it was limited to standalone elastic band structures rather than coupled multi-elastic components [27]. Current models generally suffer from two issues limitations: first, simplifying heterogeneous components as ideal springs in series using linear models, thereby neglecting nonlinearities under large deformations; second, employing numerical simulations that, while capable of modeling specific designs, fail to provide generalized design principles, compelling researchers to rely on computationally intensive parameter scanning and iterative trial-and-error.

Inspired by the functional morphology of the springtail's furcula, which utilizes coupled rotational and bending deformations for energy storage and release, we developed a series elastic actuator (SEA). This design structurally mimics the springtail by integrating double-torsion springs to replicate the furcula's rotational kinematics and carbon-fiber strips to emulate its bending deformation, capturing the essence of its composite deformation mechanism. The main contributions are as follows:

1) *Bio-inspired Design Strategy:* We translated the springtail's composite deformation mechanism—the concurrent presence of rotational and bending modes in its jumping organ—into a robotic SEA architecture. This is achieved through a triple-stage series configuration combining double-torsion springs (rotational deformation) and carbon-fiber strips (bending deformation), enabling enhanced elastic energy storage through the synergistic use of distinct deformation modes.
2) *Theoretical Contribution:* We present a unified axial force model for series-elastic systems coupling torsion springs and carbon-fiber strips. The model characterizes strain coordination between heterogeneous elastic elements.
3) *Mechanistic Insight:* We experimentally validate the mechanical compatibility between nonlinear and linear elastic elements in series, achieving a force coupling deviation below 4.4% across the operational range through parameter optimization.

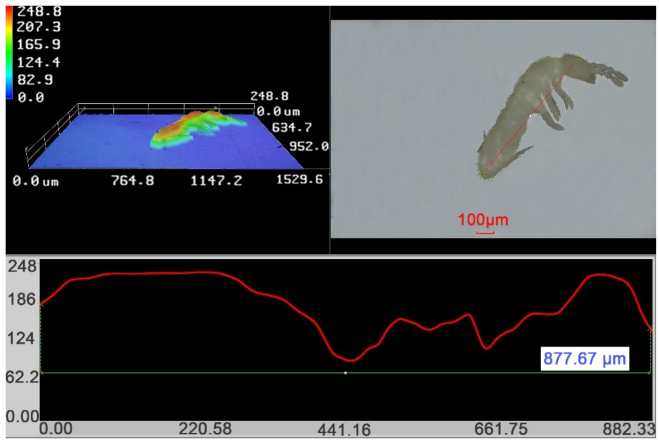

Fig. 1. Morphological characteristics of springtails.

4) *Performance of the TCS-Jumper:* The TCS-Jumper prototype demonstrated a vertical jump height of 3.5 m, an energy storage capacity of 28 J (140 J/kg), and a gravitational potential energy conversion efficiency of 65.4%.

II. Structural Design of Series-Elastic Actuator

A. Morphological Characteristics of Springtails

Springtails are minute arthropods with a small body divided into head, thorax, and abdomen. Their defining feature is the terminal abdominal jumping organ (furcula), composed of two parts: the manubrium and dens. At rest, it folds into a ventral groove, acting as a spring storing elastic energy. Fig. 1 shows the structure of a springtail photographed using an Easy Zoom5 super-depth microscope.

B. Synergistic Deformation Mechanism of the Springtail Furcula

The jumping performance of springtails is governed by the complex composite deformation of their furcula, which involves both rapid flipping (rotation) and controlled bending. Oliveira et al. elucidated springtail jumping dynamics, identifying that energy transmission efficiency is critically determined by the coupled elastic deformation at the dens-manubrium joint [28]. High-speed imaging revealed that ground contact induces joint flexion (bending) triggered by the furcula's rotation (Fig. 2). This synergistic coupling of bending and rotational deformations enables efficient energy storage and release, providing bio-inspired solutions for high-performance elastic actuators.

C. Springtail Inspired Series Elastic Actuator Design

Inspired by the energy release mechanism in springtails, we present a novel SEA featuring a symmetric configuration. The architecture comprises a centrally positioned carbon-fiber strip symmetrically coupled to double-torsion springs at each terminal. Mechanically, the double-torsion springs replicate the rotational kinematics of the springtail's manubrium through torsion, while the carbon-fiber strip mimics the furcula's energy

IEEE Robotics and Automation Letters (RA-L) paper, presented at ICRA 2026, Vienna, Austria. Cite as RA-L paper.

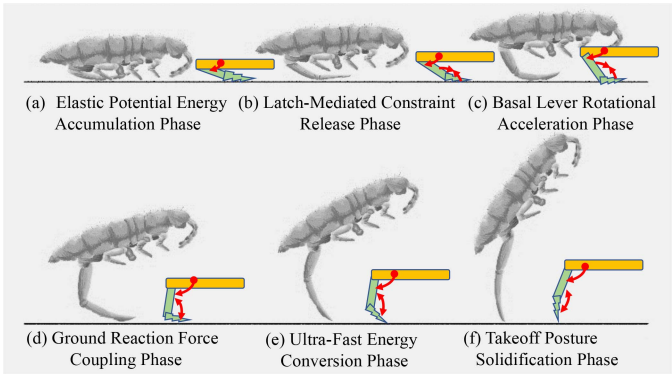

Fig. 2. Schematic of springtail jumping sequence. (a) Initial state: dens-manubrium joint in near-linear configuration. (b) Release Initiation: mucro initiates ground contact. (c) Acceleration Phase: ground reaction force transmission to the caudal region induces initial flexion at the dens-manubrium joint. (d) Coupling Phase: progressive flexion deformation intensification at the joint. (e) Energy release phase: furcula reverts from flexed state to linear conformation. (f) Takeoff posture: furcula restored to near-linear state.

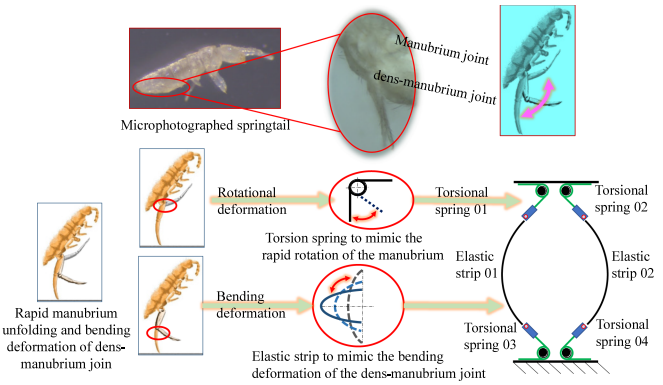

Fig. 3. Structural design of the SEA inspired by the springtail hierarchical energy release mechanism.

storage behavior via bending deformation. This biomimetic design effectively captures the dynamic energy storage-release characteristics of springtail locomotion. The symmetric parallel arrangement achieves mechanical coupling that enhances energy density, structural stability, and load-bearing capacity, as validated in Fig. 3.

D. Force Model of Carbon-Fiber Strip

The carbon-fiber strip, symmetrically fixed to double-torsion springs at both ends, undergoes neutral axis offset under axial tension F. This induces arcuate curvature via buckling (Fig. 4(a)), with termini experiencing equal opposing forces (F_5, F_6) directed toward the curvature center – a two-force equilibrium.

E. Force Model of Double-Torsion Springs

As linear-elastic auxiliary energy storage elements, each spring's free end connects to the carbon-fiber strip via pinned joint, while fixed ends attach to the frame. Axial loading generates reaction forces at joints (F_5, F_5' in Fig. 4(a)), equal in magnitude but opposite to the carbon-fiber strip's axial force.

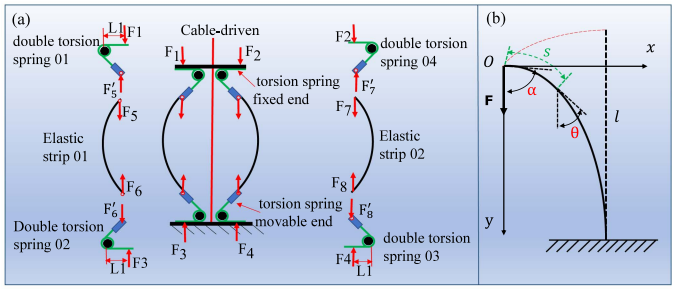

Fig. 4. Mechanical analysis model of series-elastic actuators. (a) Force models of novel SEA and it's components. (b) Large deformation model of carbon-fiber strip.

Torsional deformation produces a vertically downward concentrated force at the fixed end, forming a self-equilibrating force pair (F_1, F_5') to achieve spatial equilibrium.

F. Force Model of Novel SEA

In the proposed SEA, a mechanical coupling arises between the torsional deformation of the double-torsion springs and the bending deformation of the carbon-fiber strip. Bending deflection of the carbon-fiber strip induces angular displacement in the double-torsion springs through nodal reaction forces, while the restorative torque of the springs reciprocally applies counterforce on the carbon-fiber strip. This bidirectional coupling creates a composite torsion-bending energy transduction pathway. Based on the established carbon-fiber strip mechanics and double-torsion spring force model, the novel SEA force model (Fig. 4) was formulated to comprehensively characterize force transmission and energy conversion between heterogeneous elastic components.

III. Modeling of Series-Elastic Actuator

A. Large Deformation Model for Carbon-Fiber Strip

Consider a homogeneous carbon-fiber strip (initial length L_0, width b, thickness h, moment of inertia $I = bh^3/12$) under opposing axial forces F, α is the angle formed at the end point of the carbon-fiber strip, and θ is the angle between the tangent line of the deflection curve and the y-axis. Based on the symmetry relationship, we consider the half-length segment $l = L_0/2$; this segment is modeled as an ideal carbon-fiber strip with one end fixed and the axial force F applied at the free end (Fig. 4(b)). When $F > F_{cr}$ (F_{cr} denotes the critical force during a large deformation), large-deflection bending occurs, the parameter description of shrapnel is shown in Table II. According to the expression of curvature: $1/\rho = -\mathrm{d}\theta/\mathrm{d}s$ (negative as θ decreases with s) and from bending theory $1/\rho = M/E_C I$, the equilibrium equation can be expressed as follows:

$$\frac{F \cdot x}{E_C \cdot I} + \frac{d\theta}{ds} = 0 \tag{1}$$

Let $k = \sqrt{\frac{F}{E_C \cdot I}}$

IEEE Robotics and Automation Letters (RA-L) paper, presented at ICRA 2026, Vienna, Austria. Cite as RA-L paper.

TABLE II
MATERIAL PARAMETERS OF CARBON-FIBER STRIP

Parameter	Value	Unit	Physical meaning
ρ	-	m	Radius of curvature
θ	-	rad	Rotation angle
S	-	m	Arc length
M	-	N·m	Bending moment
I	-	m^4	Bending rigidity
F	-	N	Axial force
x	-	m	Axial displacement
L_0	0.3	m	Length
b	25	mm	Width
h	1.8	mm	Thickness
E_C	45×10^9	Pa	Carbon fiber elastic modulus
I	$bh^3/12$	m^4	Section moment of inertia
$\alpha_{\max}$	$\pi/2$	rad	Maximum angle (radians)

Differentiating both sides of (1) with respect to s yields the following governing equation of the deflection curve:

$$\frac{d^2\theta}{ds^2} + k^2 \sin\theta = 0 \tag{2}$$

Let $p = \frac{d\theta}{ds}$.

Integrating both sides yields the following:

$$p = \sqrt{2k^2 \cos\theta + 2C} \tag{3}$$

Next, the boundary conditions at the free end of the carbon-fiber strip are as follows:

$$\theta\big|_{s=0} = \alpha, \quad \left.\frac{d\theta}{ds}\right|_{s=0} = 0 \tag{4}$$

Substituting the boundary conditions into (3) yields the following:

$$ds = \frac{1}{2k\left(\sin^2\frac{\alpha}{2} - \sin^2\frac{\theta}{2}\right)} d\theta \tag{5}$$

Integrating both sides of (5) yields the following:

$$l = \frac{1}{2k}\int_0^{\alpha} \frac{1}{\sqrt{\sin^2\frac{\alpha}{2} - \sin^2\frac{\theta}{2}}} d\theta \tag{6}$$

To simplify the preceding integral, a new variable $q = \sin\frac{\alpha}{2}$ is introduced, and we obtain the following:

$$\sin\frac{\theta}{2} = q\sin\phi = \sin\frac{\alpha}{2}\sin\phi \tag{7}$$

Substituting (7) into (6) and rearranging the equation yields the following:

$$l = \frac{1}{k}\int_0^{\frac{\pi}{2}} \frac{1}{\sqrt{1 - q^2\sin^2\phi}} d\phi = \frac{1}{k}K(p) \tag{8}$$

where $K(p) = \int_0^{\frac{\pi}{2}} \frac{1}{\sqrt{1-q^2\sin^2\phi}} d\phi$ denotes the complete elliptic integral of the first kind.

When deformation initiates, α and q asymptotically approach zero yielding:

$$l = \frac{1}{k}\cdot\int_0^{\frac{\pi}{2}} d\phi = \frac{\pi}{2}\sqrt{\frac{E_C I}{F}} \tag{9}$$

$$F_{cr} = \frac{\pi^2 E_C I}{4l^2} \tag{10}$$

Bending deformation occurs only when the axial compressive force F exceeds this critical value F_{cr}. In addition, from Fig. 4(b), we obtain:

$$dy = \cos\theta ds = \frac{\cos\theta}{2k\sqrt{\sin^2\frac{\alpha}{2} - \sin^2\frac{\theta}{2}}} d\theta \tag{11a}$$

$$dx = \sin\theta ds = \frac{\sin\theta}{2k\sqrt{\sin^2\frac{\alpha}{2} - \sin^2\frac{\theta}{2}}} d\theta \tag{11b}$$

The transformation of the integration limit of (11) yields the following:

$$y = \frac{2l}{K(p)}E(p) - l \tag{12}$$

where $E(p) = \int_0^{\frac{\pi}{2}} \sqrt{(1 - \sin^2\frac{\alpha}{2}\cdot\sin^2\phi)} d\phi$ denotes the complete elliptic integral of the second kind.

A carbon-fiber strip was arranged on both sides in mirror symmetry in the novel SEA. Consequently, the resultant axial force $F_{2C\text{-}axial}$ was twice the axial compressive force $F_{C\text{-}axial}$ of a single carbon-fiber strip. The axial displacement Δy_C is defined as the difference between the original length L_0 and the deformed axial length. In (12), the axial length y is derived from the characteristic dimension ($L_0 = 2l$). By (8) and (12), a nonlinear parametric equation relating $F_{2C\text{-}axial}$ and Δy_C is established as follows:

$$\begin{cases} F_{2C\text{-}axial} = 8\left(\frac{K(\sin\frac{\alpha}{2})}{L_0}\right)^2 E_C I \\ \Delta y_C = 2L_0\left(1 - \frac{E(\sin\frac{\alpha}{2})}{K(\sin\frac{\alpha}{2})}\right) \end{cases} \tag{13}$$

The nonlinear force displacement relationship of the carbon-fiber strip (13) explained the hierarchical energy release process during the bending deformation of the springtail's dens-manubrium joint (Fig. 2(c)–(e)). The carbon-fiber strip used its hyperelastic and ultra-low-density characteristics to accomplish the dual objectives of enhanced energy storage density and rapid dynamic response speed. The carbon-fiber strip material parameters are listed in Table II.

B. Torsion Spring Linear Elastic Model

Elasticity equation for double-torsion spring:

$$T_{DTS} = \frac{E_{TS} d^4 \alpha}{32nD} \tag{14}$$

The parameter of the double-torsion spring is shown in Table III.

The symmetrically arranged double-torsion springs on both sides of the carbon-fiber strip exhibit twice the axial force magnitude of a single spring. Per Section II-E force analysis, the resultant axial force $F_{2DTS-axial}$ at the springs' active ends relates to their torque T_{DTS} as:

$$F_{2DTS\text{-}axial} = \frac{2T_{DTS}}{L_{D\text{-}TS}} = \frac{E_{TS} d^4 \alpha}{16nDL_{D\text{-}TS}\sin\alpha} \tag{15}$$

IEEE Robotics and Automation Letters (RA-L) paper, presented at ICRA 2026, Vienna, Austria. Cite as RA-L paper.

TABLE III
DOUBLE-TORSION SPRING PARAMETERS

Parameter	Value	Unit	Physical meaning
M	-	N·m	Torque of the torsion spring
L_{D-TS}	46	mm	Moment arm of torsion spring
n	2	-	Number of active coils
d	1.8	mm	Wire diameter
D	13	mm	Mean coil diameter (mm)
E_{TS}	200×10^9	Pa	Elastic modulus
α	-	rad	Torsional angle (radians)

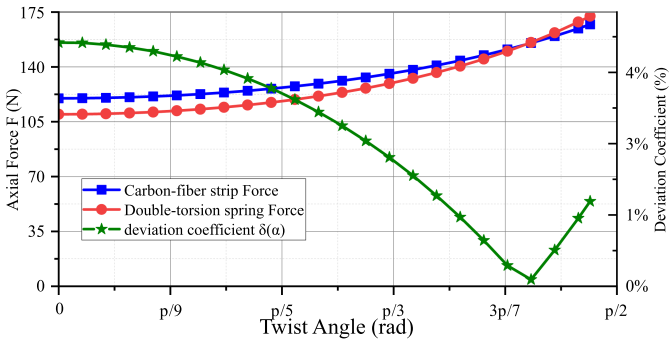

Fig. 5. Mechanical compatibility of carbon-fiber strip and double-torsion springs: axial force coordination and quantitative deviation analysis.

In the novel SEA, both ends of the carbon-fiber strip were firmly connected to the double-torsion springs. Therefore, the axial displacement expression of the movable end of the double-torsion spring Δy_{TS} can be expressed as follows:

$$\Delta y_{TS} = 2L_{D\text{-}TS}\,(1 - \cos\alpha) \tag{16}$$

C. Unified Axial Force Model

Per Section III-A carbon-fiber strip model and Section III-B double-torsion spring analysis, both axial forces can be expressed as α-dependent functions:

$$F_{total\text{-}axial}(\alpha) = \begin{cases} F_{2C\text{-}axial}(\alpha) = 8\left(\frac{K(\sin\frac{\alpha}{2})}{L_0}\right)^2 E_C I & \text{(strip)} \\ F_{2DTS\text{-}axial}(\alpha) = \frac{E_{TS}\cdot d^4\cdot\alpha}{16nD\cdot L_{D\text{-}TS}\cdot\sin\alpha} & \text{(torsion)} \end{cases} \tag{17}$$

D. Matching Criteria

Dynamic response comparison (Fig. 5) reveals enhanced convergence of $F_{2C-axial}(\alpha)$ and $F_{2DTS-axial}(\alpha)$ curves, indicating superior system synergy. The normalized deviation coefficient $\delta(\alpha)$ defines mechanical matching:

$$\delta(\alpha) = \frac{|F_{2C\text{-}axial}(\alpha) - F_{2DTS\text{-}total}(\alpha)|}{F_{2C\text{-}axial}(\alpha) + F_{2DTS\text{-}total}(\alpha)} \times 100\% \tag{18}$$

The normalized mean deviation coefficient is expressed as follows:

$$\overline{\delta(\alpha)} = \sqrt{\frac{1}{N}\sum_{i=1}^{N}\left(\frac{F_{2C\text{-}axial}(\alpha) - F_{2DTS\text{-}total}(\alpha)}{F_{2C\text{-}axial}(\alpha) + F_{2DTS\text{-}total}(\alpha)}\right)^2} \tag{19}$$

As demonstrated in Fig. 5, mechanical compatibility between the carbon-fiber strip and double-torsion springs was evaluated of a torsion angle range of$\alpha \in [0, \pi/2]$. The carbon-fiber strip exhibited axial force progression from 119.9N to 167.1N, while the double-torsion spring demonstrated a corresponding increase from 109.7N to 172.3N. The components displayed highly consistent force-displacement behaviors, with near identical profiles indicating superior mechanical synchronization. This alignment confirms minimal energy dissipation during deformation. Quantitative mechanical matching was assessed through deviation coefficient $\delta(\alpha)$ analysis, revealing a maximum deviation coefficient δ_{max} of 4.44% and a mean deviation coefficient $\overline{\delta(\alpha)}$ of 2.7% across the operational range.

E. Analysis of Novel SEA

Both ends of the carbon-fiber strip are securely connected to the double-torsion springs, with the angle α remaining consistent between the two components. Previous analysis indicates that within the range $[0, \pi/2]$, the deviation between $F_{2C\text{-}axial}(\alpha)$ and $F_{2DTS\text{-}axial}(\alpha)$ consistently remains below 4.44%. Therefore, the axial force of the novel SEA system can be approximated as $F_{2C\text{-}axial}$. On the other hand, the axial displacement Δy of the novel SEA system combined the superposition effect of the bending deformation Δy_C in the carbon-fiber strip and the torsional deformation Δy_{TS} in the double-torsion springs. In summary, the analytical expressions for the system's axial resultant displacement and axial resultant force can be expressed as follows:

$$\begin{cases} F_{total} = 8\left(\frac{K(\sin\frac{\alpha}{2})}{L_0}\right)^2 E_C I \\ \Delta y = 2L_0\left(1 - \frac{E(\sin\frac{\alpha}{2})}{K(\sin\frac{\alpha}{2})}\right) + 2\cdot L_{D\text{-}TS}\cdot(1-\cos\alpha) \end{cases} \tag{20}$$

The proposed novel SEA elastic energy storage capacity can be expressed as the sum of the carbon-fiber strip and the double-torsion springs:

$$U_{total}(\alpha) = \underbrace{\int_0^{\Delta y_C} 16L_0E_CI\left(\frac{K(\sin\frac{\alpha}{2})}{L_0}\right)^2 d\left(1 - \frac{E(\sin\frac{\alpha}{2})}{K(\sin\frac{\alpha}{2})}\right)}_{U_{CF}(elasticstrips)} + \underbrace{\frac{E_{TS}\cdot d^4\cdot\alpha^2}{32\cdot n\cdot D}}_{U_{TS}(TorsionSpring)} \tag{21}$$

The novel SEA system's initial axial force was 120 N at torsion angle $\alpha = 0$, increasing to 167N at $\alpha = \pi/2$ (Fig. 6(a)). Throughout the entire deformation range, the carbon fiber strips and double-torsion springs maintain a dynamic equilibrium in energy storage distribution, with the carbon fiber strips accounting for approximately 64% and the double-torsion springs for approximately 36%. Compared to equivalent alternative actuators that utilize only a single component, this structure not only offers significant advantages in energy storage, but also effectively enhances the reliability and fatigue performance of the system through its load-sharing mechanism.

IEEE Robotics and Automation Letters (RA-L) paper, presented at ICRA 2026, Vienna, Austria. Cite as RA-L paper.

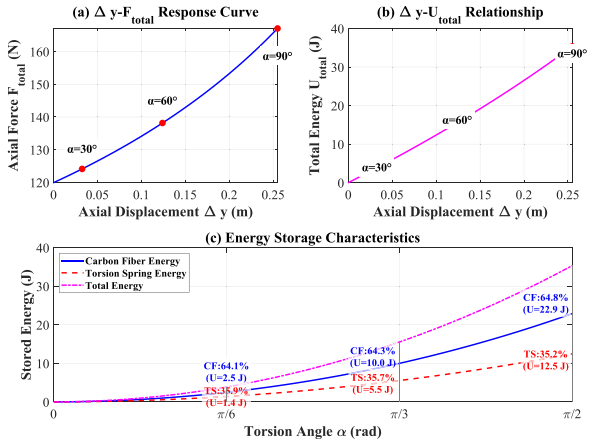

Fig. 6. Analysis of novel SEA. (a) Axial force characteristic curve of the novel SEA. (b) Novel SEA energy storage curve with displacement. (c) Comparison of energy storage characteristics between carbon-fiber strip, double-torsion springs, and novel SEA.

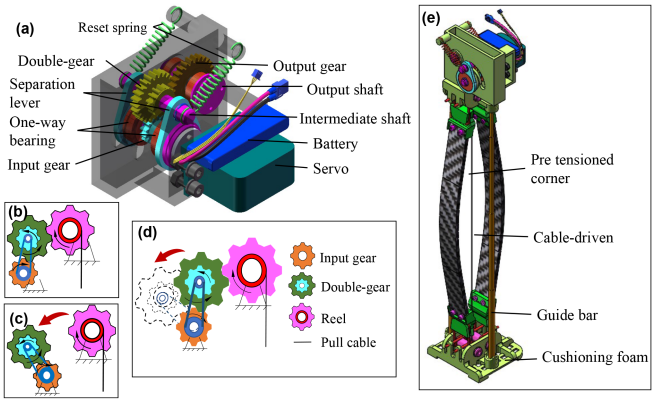

Fig. 7. Prototype design. (a) Overall structure of drive and transmission system. (b) Transition gear maintaining engagement with double-gear. (c) Transition gear disengagement from double-gear. (d) Schematic of separation lever driving transition gear engagement/disengagement. (e) 3D prototype model of jumping robot.

IV. Prototype Design and Experimentation

A. Energy Storage and Release Control

The proposed novel series elastic actuator (SEA) system achieves energy management through a dual-gear mechanism under reset spring preload. During energy storage, the servo motor drives the driver gear in clockwise rotation, transmitting motion through the gear train to synchronize the driven gear and cable spool. As the traction cable winds orderly onto the spool, the SEA undergoes axial compression, accumulating elastic potential energy in the SEA system. (Fig. 7). For energy release, the servo motor drive one-way clutch actuates the separation lever to disengage the output gear from the dual-gear set, triggering rapid conversion of stored elastic potential energy into kinetic energy through ground reaction forces. This process completes the vertical jump motion within milliseconds, demonstrating efficient energy transduction.

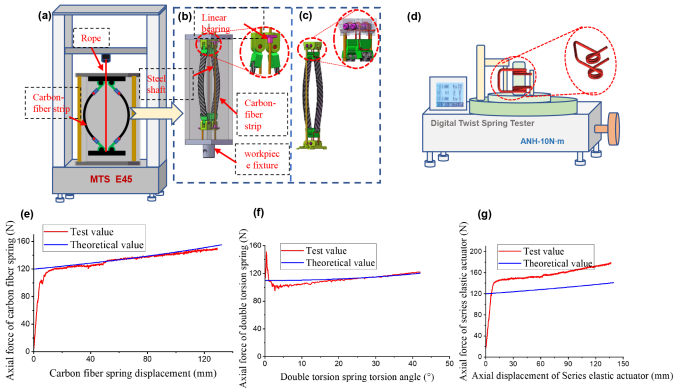

Fig. 8. Mechanical property testing of carbon-fiber strip and double-torsion spring. (a) Experiment apparatus for carbon-fiber strip and novel SEA system. (b) Experiment mechanism for carbon-fiber strip. (c) Experiment mechanism for novel SEA system. (d) Experiment scheme for double-torsion spring. (e) Experimental vs. theoretical values for carbon-fiber strip. (f) Experimental vs. theoretical values for double-torsion spring.

B. Component Testing

Experimental validation was conducted to characterize mechanical behaviors of the carbon-fiber strip, double-torsion springs, and integrated SEA system. Key equipment included: 1) MTS Exceed E45 testing machine; 2) Digital torsion spring tester; 3) Custom SEA test fixture mounted on the universal tester.

1) *Carbon-fiber strip testing:* The carbon-fiber strips, arranged in a mirror-symmetric configuration with hinged connections, were mounted between upper/lower frames. The universal tester elevated the lower frame at a constant speed while recording axial force-displacement data at 500 Hz (Fig. 8(a)–(b)).
2) *Double-torsion spring testing:* The spring's fixed end was secured via the tester's stop pin, while the free end was attached to the torsion fork. Manual loading induced controlled torsional deformation at uniform rotational speed, with real-time torque-angle data acquisition forming complete characteristic curves (Fig. 8(d)).

The axial force displacement characteristics of the carbon-fiber strip were tested using an MTS testing machine, as shown in Fig. 8(e). The following results were obtained: During the carbon-fiber strip testing, the force increased at a relatively slow rate in the small-deformation region ($\Delta y_C < 9$ mm), with an average error of 19.1%. Which was primarily attributed to three factors with their respective contributions: rope flexibility (36.74%), guidanceangle effects (26.49%), and joint clearance together with other factors (36.77%). Specifically, the minor guidance angle induced an initial soft response; the accumulated clearance in multiple joints led to nonworking displacement; and the initial plastic deformation of the ropes further delayed the force response. In contrast, within the large-deformation range (9 mm $< \Delta y_C <$ 163 mm), the system entered a stable deformation state where the influence of initial imperfections and clearances diminished. In this regime, the experimental data aligned closely with theoretical predictions, exhibiting an

IEEE Robotics and Automation Letters (RA-L) paper, presented at ICRA 2026, Vienna, Austria. Cite as RA-L paper.

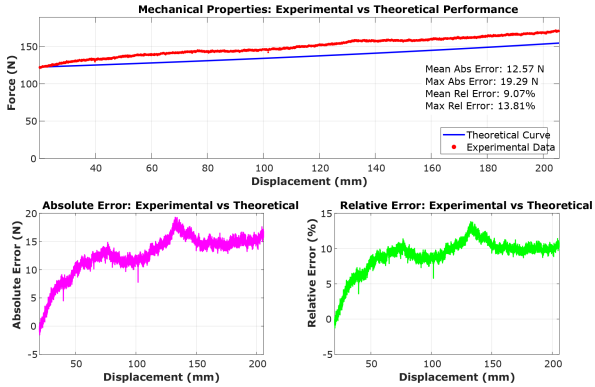

Fig. 9. Comparison of theoretical and test data of the series-elastic actuator for displacements ranging from 20 to 241 mm.

average error of less than 3.87% and maintaining a strong linear correlation.

The torque-angle characteristics of the double-torsion spring were measured using an ANH-10 $\mathrm{N}\cdot\mathrm{m}$ digital display torsion spring tester. Torque-angle curves were recorded at various rotation angles α, and the data were subsequently converted into axial force-angle curves using (15), as illustrated in Fig. 8(f). The analysis revealed significant errors between the measured and theoretical values in the low-rotation-angle region ($\alpha < 5^\circ$), with an average error of 8.4%. In contrast, in the high-rotation-angle region ($\alpha > 5^\circ$), the experimental results demonstrated excellent agreement with the theoretical model, exhibiting an average error of only 2.1%.

C. SEA Testing

The novel SEA mechanical characterization followed identical method to those used in carbon-fiber testing, with the critical distinction lying in the double-torsion spring connection methodology (Fig. 8(a) and (c)). Fig. 9 illustrates the novel SEA system's mechanical response characteristics. We conducted 10 sets of repeatability tests, key performance metrics included: Maximum axial force difference: 12.17 N (9.93% error), average axial force difference: 4.68 N (3.22% error). In the small-deformation regime ($\Delta y_C < 20$ mm), the experimental force exhibited a gradual increase with limited statistical significance, which we attribute to systematic mechanism errors discussed in the preceding section. For large deformations (20 mm $< \Delta y_C <$ 241 mm), the error displayed a distinct progression: it decreased sharply from 9.93% to approximately 1% within the 20-50 mm range, stabilized below 1% throughout the 50-100 mm range, then gradually increased to around 5% during the 100-200 mm range, eventually converging to a stable value of approximately 5%. The average error between experimental measurements and theoretical predictions was 3.22%, while maintaining strong linear correlation.

D. Jumping Performance Experimental

A testing platform was constructed to evaluate the TCS-Jumper prototype's locomotion capabilities. The aluminum-alloy framework measured 5.0 m (height) $\times$ 1.5 m (length) $\times$ 1.5 m (width), with the base incorporating foam cushioning to mitigate landing impacts.

TABLE IV
MASS BUDGET OF PROTOTYPE

Component	Mass (g)	Qty.	Total Mass (g)
Frame	58.3	1	58.3
Servo	68.3	1	68.3
Battery	90	1	90
Reset spring	0.8	2	1.6
Input shaft	3.6	1	3.6
Intermediate shaft	2.2	1	2.2
Output shaft	24.8	1	24.8
Input gear	3.4	1	3.4
Twin gear	15.1	1	15.1
Output gear	17.4	1	17.4
One-way bearing	15	2	30
Separation pendulum	8.6	2	17.2
Bearing	1.4	4	5.5
Screw	1.3	10	13
Circlip	0.3	14	4.6
Double-torsion spring	3.5	4	13.8
Carbon-fiber strip	24	2	47.5
Connecting piece	7.1	4	28.4
Straight shaft	3	4	12.2
Guide bar	35	2	35
Support bracket	30.3	1	30.3
Cushioning foam	11.8	1	11.8
Total			534

TABLE V
PROTOTYPE JUMPING EXPERIMENT

Jump Height	Average jump height	Standard Deviation(s)	Ideal Jump Height	η (%)
H (m)	3.50 $\pm$ 0.05 m	0.0913	5.35	65.4

During experimental trials, the prototype adopted an upright initial posture. Elastic potential energy was stored through remote-controlled servo motor actuation, which compressed the SEA. Upon reaching a compression ($\Delta y = 208.23$ mm), the servo motor reversed direction via remote trigger, disengaging the output gear and enabling rapid energy release. High-speed cameras synchronized with the release event recorded the complete trajectory from energy discharge to peak height attainment. The prototype's mass distribution is detailed in Table IV.

The target jumping height is the height achieved when all elastic potential energy is converted into gravitational potential energy under the condition of no energy loss and elastic-gravitational energy conversion efficiency. The conversion of elastic potential energy to gravitational potential energy is calculated as follow:

$$\eta = \frac{mgH}{E_{spring}} \times 100\% \quad \left(E_{spring} = \int_0^{\Delta y} F_{total} dy \right) \tag{22}$$

Jumping performance was evaluated through 10 independent trials. yielding a mean jump height of 3.50 m $\pm$ 0.05 m, the reported value represents the average jumping height across all trials, with individual peak values ranging from 3.35-3.65 m, as shown in Table V.

As illustrated in Fig. 10(a), theoretical predictions (blue curve) and experimental measurements (red fitted line overlaid

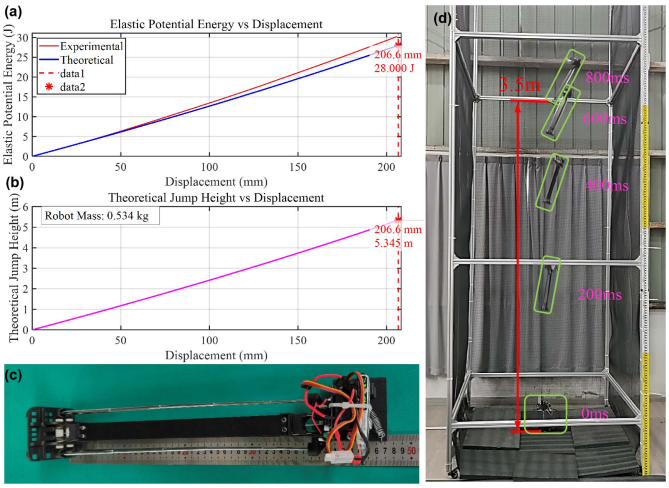

Fig. 10. Jumping robot prototype's performance. (a) Comparison curve of theoretical and experimental stored energy. (b) Relationship between theoretical jumping height and deformation. (c) Physical image of the spring-powered jumping robot. (d) Image of the jumping experiment.

on discrete data points) both demonstrate quasi-linear growth characteristics across the 0-208.23 mm compression stroke interval. At maximum compression (208.23 mm), the system achieves 28.42 J of measured stored energy versus 28 J theoretical energy storage. This corresponds to an actual jump height of 3.5 m (Fig. 10(d)), with gravitational potential energy at apex reaching 18.3 J. The effective energy conversion efficiency from elastic potential to gravitational potential energy was calculated at 65.4%, yielding a theoretical jump height projection of 5.345 m based on the 0.534 kg system mass.

The observed discrepancy between experimental outcomes and theoretical model predictions (Fig. 10(b)) arise from two principal factors: 1) cumulative energy losses from elastic actuator internal friction and aerodynamic drag forces, which significantly degrade vertical jump performance; 2) reduced effective energy conversion efficiency due to increased foot mass ratio during takeoff phase.

V. Conclusion

This letter presents a bio-inspired series elastic actuator (SEA) that integrates double-torsion springs and carbon-fiber strips to emulate the deformation coupling observed in springtails. A unified axial force model was developed to characterize the mechanical compatibility between linear and nonlinear elastic elements, achieving a maximum force deviation of 4.4% across the operational range. Experimental results demonstrate that the TCS-Jumper prototype achieves a mean jump height of 3.5 m with high energy density and conversion efficiency.

References

[1] D. W. Haldane and R. S. Fearing, "Robotic vertical jumping agility via series-elastic power modulation," *Sci. Robot.*, vol. 1, no. 1, 2016, Art. no. eaag2048.
[2] J. Zhao et al., "Scout robot with wheeling-hopping combination locomotion," *Ind. Robot: Int. J.*, vol. 36, no. 3, pp. 244–248, 2009.
[3] J. Burdick et al., "Minimalist jumping robots for celestial exploration," *Int. J. Robot. Res.*, vol. 22, no. 8, pp. 653–674, 2003.
[4] R. Blickhan et al., "Similarity in multilegged locomotion: Bouncing like a monopode," *J. Comp. Physiol. A*, vol. 173, no. 5, pp. 509–517, 1993.
[5] C. Zhang et al., "Biologically inspired jumping robots: A comprehensive review," *Robot. Auton. Syst.*, vol. 124, 2020, Art. no. 103362.
[6] Y. Yang, Z. Feng, S. Ma, L. Tang, C. Jin, and Y. Li, "The continuous jump control of a locust-inspired robot with omnidirectional trajectory adjustment," *IEEE Robot. Autom. Lett.*, vol. 9, no. 3, pp. 2040–2047, Mar. 2024.
[7] Y. Pan et al., "Tumro: A tunable multimodal wheeled jumping robot based on the bionic mechanism of jumping beetles," *Adv. Intell. Syst.*, vol. 6, no. 2, 2024, Art. no. 2400024.
[8] Z. Zhou et al., "Self-sustained and coordinated rhythmic deformations with SMA for controller-free locomotion," *Adv. Intell. Syst.*, vol. 6, no. 2, 2024, Art. no. 2300667.
[9] Z. Zhang et al., "A survey of bioinspired jumping robot: Takeoff, air posture adjustment, and landing buffer," *Appl. Bionics Biomech.*, vol. 2017, pp. 1–22, 2017.
[10] E. W. Hawkes et al., "Engineered jumpers overcome biological limits via work multiplication," *Nature*, vol. 604, no. 7907, pp. 657–661, 2022.
[11] G.-P. Jung, C. S. Casarez, S.-P. Jung, R. S. Fearing, and K.-J. Cho, "An integrated jumping-crawling robot using height-adjustable jumping module," in *Proc. IEEE Int. Conf. Robot. Automat.*, Sweden, 2016, pp. 4680–4685.
[12] G.-P. Jung et al., "JumpRoACH: A trajectory-adjustable integrated jumping-crawling robot," *IEEE/ASME Trans. Mechatron.*, vol. 24, no. 3, pp. 947–958, Jun. 2019.
[13] A. Yamada et al., "Asymmetric robotic catapults based on the closed elastica for jumping robot," *J. Robot. Soc. Jpn.*, vol. 26, no. 4, pp. 363–371, 2008.
[14] A. Yamada, H. Mameda, H. Mochiyama, and H. Fujimoto, "A compact jumping robot utilizing snap-through buckling with bend and twist," in *Proc. IEEE/RSJ Int. Conf. Intell. Robots Syst.*, Taipei, Taiwan, 2010, pp. 389–394.
[15] J. Zhao, N. Xi, B. Gao, M. W. Mutka, and L. Xiao, "Design and testing of a controllable miniature jumping robot," in *Proc. RSJ Int. Conf. Intell. Robots Syst.*, Taipei, Taiwan, 2010, pp. 3346–3351.
[16] J. Zhao et al., "MSU jumper: A single-motor-actuated miniature steerable jumping robot," *IEEE Trans. Robot.*, vol. 29, no. 3, pp. 602–614, Jun. 2013.
[17] J. Zhao, T. Zhao, N. Xi, M. W. Mutka, and L. Xiao, "MSU tailbot: Controlling aerial maneuver of a miniature-tailed jumping robot," *IEEE/ASME Trans. Mechatron.*, vol. 20, no. 6, pp. 2903–2914, Dec. 2015.
[18] Y. Ma et al., "A biologically inspired height-adjustable jumping robot," *Appl. Sci.*, vol. 11, no. 11, 2021, Art. no. 5167.
[19] C. Hong et al., "A combined series-elastic actuator & parallel-elastic leg no-latch bio-inspired jumping robot," *Mechanism Mach. Theory*, vol. 149, 2020, Art. no. 103814.
[20] J. Lo et al., "Characterising the take-off dynamics and energy efficiency in spring-driven jumping robots," *Mechanism Mach. Theory*, vol. 199, 2024, Art. no. 105688.
[21] D. W. Haldane, J. K. Yim, and R. S. Fearing, "Repetitive extreme-acceleration (14-g) spatial jumping with Salto-1P," in *Proc. IEEE/RSJ Int. Conf. Intell. Robots Syst.*, Vancouver, BC, Canada, 2017, pp. 3345–3351.
[22] M. A. Woodward et al., "MultiMo-Bat: A biologically inspired integrated jumping-gliding robot," *Int. J. Robot. Res.*, vol. 33, no. 12, pp. 1511–1529, 2014.
[23] J. Dong et al., "Design, analysis, and tests of an impulsive aquatic jumping mechanism inspired by frog limbs," *IEEE Robot. Autom. Lett.*, vol. 9, no. 7, pp. 6344–6351, Jul. 2024.
[24] Y. Xu et al., "Design and optimization of a miniature locust-inspired stable jumping robot," *IEEE Robot. Autom. Lett.*, vol. 8, no. 8, pp. 4673–4680, Aug. 2023.
[25] R. Sato et al., "Vertical jumping by a legged robot with upper and lower leg Bi-articular muscle-tendon complexes," *IEEE Robot. Autom. Lett.*, vol. 6, no. 4, pp. 7572–7579, Oct. 2021.
[26] F. R. Serrano et al., "A springtail-inspired multimodal walking-jumping microrobot," *Sci. Robot.*, vol. 10, no. 99, 2025, Art. no. eadp7854.
[27] J. Zhao, W. Yan, N. Xi, M. W. Mutka, and L. Xiao, "A miniature 25 grams running and jumping robot," in *Proc. IEEE Int. Conf. Robot. Automat.*, Hong Kong, SAR, China, 2014, pp. 5115–5120.
[28] F. G. L. Oliveira et al., "A morphofunctional study of the jumping apparatus in globular springtails," *Arthropod Struct. Develop.*, vol. 79, 2024, Art. no. 101333.